A TWO-COLOR MAP OF PLUTO'S SUB-CHARON HEMISPHERE

ELIOT F. YOUNG
Southwest Research Institute, Department of Space Studies, Boulder, CO 80302; efy@everest.boulder.swri.edu

RICHARD P. BINZEL
Massachusetts Institute of Technology, Department of Earth, Atmospheric, and Planetary Science, Cambridge, MA 02139

AND

KEENAN CRANE
Boulder High School, Boulder, CO 80302

ABSTRACT

Pluto and its satellite Charon regularly occulted or transited each other's disks from 1985 through 1990. The light curves resulting from these events (collectively called "mutual events") have been used to determine albedo maps of Pluto's sub-Charon hemisphere. We now use a data set of four light curves that were obtained in both B and V Johnson filters to construct a two-color map of Pluto's surface. We are able to resolve the central part of Pluto's sub-Charon hemisphere. We find that the dark albedo feature that forms a band below Pluto's equator is comprised of several distinct color units. We detect ratios of V-filter/B-filter normal reflectances ranging from ∼1.15 to ∼1.39 on Pluto's sub-Charon hemisphere.

Key word: planets and satellites: individual (Pluto, Charon)

1. INTRODUCTION

The Pluto-Charon mutual events have been exploited for over a decade to infer an albedo distribution of Pluto's sub-Charon hemisphere (e.g., see Young et al. 1999, hereafter EY99). The basic idea is to keep track of the change in brightness of the combined Pluto-Charon system when part of Pluto is covered by Charon or its shadow. The change in brightness lets us infer the albedo of the newly covered or uncovered region on Pluto. Because Pluto and Charon are in mutually synchronous orbits, the same face of Pluto is always transited by Charon, and only the sub-Charon hemisphere of Pluto can be mapped using this technique. Previous mutual-event albedo maps have been published in Johnson B filter only. These maps show a high-contrast surface with geometric albedos ranging from 0.2 to 1 (Fig. 1). Pluto's average albedo in B is 0.5, although a nearly 30% variation is observed over Pluto's 6.38 day rotation. Pluto's $B-V$ magnitude ranges from 0.863 to 0.872 (Buie, Tholen, & Wasserman 1997a), making it one of the redder objects in the solar system. Pluto's bright surface units are primarily N_2 frost (Owen et al. 1993) with trace amounts of CO and CH_4. The compositions of the dark units are not known, but the presumption has been that these regions are colored by branched alkanes that result from UV photolysis of CH_4 (Bohn et al. 1994). The presumption is based in part on *Voyager*'s multifilter images of Triton (Fig. 2) in which reddish streaks and plume deposits are observed on older frost-covered regions (Cruikshank et al. 1998).

The Triton image shows a bright equatorial collar of recently deposited ice that is bluer than the older, dirtier ice over the southern pole. We hoped that a two-color map of Pluto could shed light on the relative ages of different frost units and perhaps confirm our expectation that the dark regions on Pluto were redder than the frost-covered regions. Although the spatial resolution of the two-color map is worse than that of our previous albedo maps (because of the small number of two-color light curves), we can show that the apparently uniform dark subequatorial band on Pluto

is actually comprised of separate red and blue regions. We are not able to resolve the color of either the south polar frost cap or the bright feature at N17° latitude, E45° longitude.

2. THE DATA SET

The four light curves used in this paper were obtained primarily by R. P. B. at the University of Texas McDonald Observatory. The detector was an RCA 8850 phototube. The observations consisted of 10 s integrations in alternating V or B filters. Figure 3 shows the $B-V$ data set, while Figure 4 shows the coverage afforded by these four events. The events are also summarized in Table 1. The total number of data points is 434.

2.1. *Coverage by the Events*

Charon's radius is slightly larger than half of Pluto's. Following Young & Binzel (1994), we have assumed 1183 km and 620 km for Pluto's and Charon's respective radii. Charon's west-to-east track across Pluto migrated from Pluto's northern to southern latitudes over the six-year mutual-event season. In theory our latitudinal resolution is determined from the overlapping event boundaries (Fig. 4), but in practice we lose the polar regions. The poles are hard to image because they are not as well illuminated as the disk center, although there is some evidence that Pluto's limb profile is flat, like the Moon's (Young & Binzel 1994), and that this is a minor effect. More important is the northward drift of Pluto's sub-Earth latitude, which means that the earlier mutual events (the ones in which Charon transited Pluto's north pole) occurred when Pluto's north pole was in darkness, just beyond the terminator, whereas later events occurred when Pluto's south pole was in darkness. Another complication is that only one of the events (1987 May 22) is complete. The middle two light curves end before their events are finished, and the fourth light curve begins in midevent. Our map-making algorithm (described in EY99) is robust in the face of missing observations, except that the
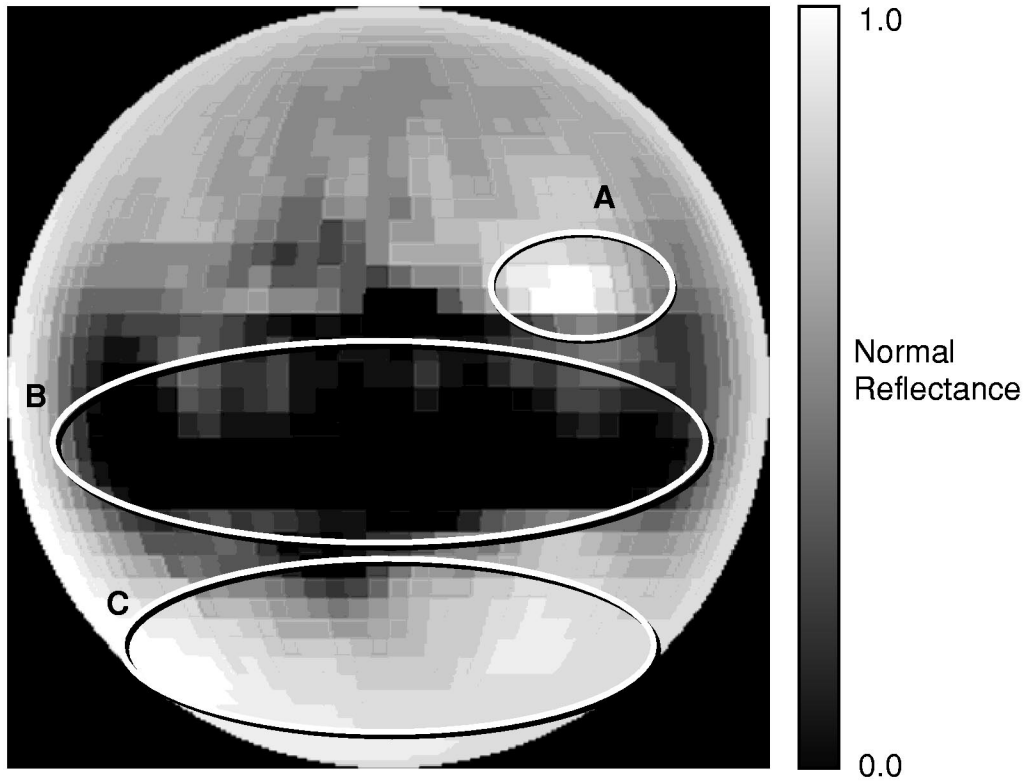
FIG. 1.—Mutual-event map of Pluto from B-filter light curves (EY99). This map, like earlier published maps (for a review, see Buie, Young, & Binzel 1997b), shows ("A") a bright frost feature at around N17°, ("B") an adjacent dark region between S40° and the equator, and ("C") a bright southern frost cap extending up to ~S40°.

regions of missing coverage will have poor spatial resolution. The area of Pluto's disk that we can resolve is only about half of what we could resolve in previous B-filter maps because of the small number of two-color events (EY99 used 18 events for their B-filter map). Nevertheless, we can show some interesting color structure in the center of Pluto's sub-Charon hemisphere.

2.2. Differences from the Single-Filter Case

A complete single-filter light curve has a U shape in which the observed light from the Pluto-Charon binary decreases by as much as 60% in the midst of an event. In contrast, the light curves in this V/B flux ratio data set are nearly flat. Working with flux ratios has advantages, such as reduced sensitivity to Pluto's opposition effect and to instantaneous Pluto-Earth separation. Most of these factors cancel out. On the other hand, the $B-V$ data set has one disadvantage; it cannot, by itself, constrain the spatial distribution of B/V flux ratios on Pluto's surface. A $B-V$ light curve does not tell us the total flux coming from Pluto in either color, but only the ratio in the two bands. When we assign V/B colors to specific locations on Pluto's surface, we will need to know the brightness of each location (in either B or V filters). Fortunately we can use previous B maps to generate that information. The process by which we turn light curves into maps involves solving a linear system of equations of the form $D(t) = Fx$, where $D(t)$ are the observations, x is a vector of unknown parameters (the "answers," or the colors of the tiles in this case), and F is the design matrix that describes how D is a linear combination of the tile colors at each of the observed time steps. The observations are not in $D(t) = Fx$ form initially. If we include Charon's contribution, the V/B flux ratio observed at time t is

$$D(t) = \frac{A_c V_c + a_1(t)V_1 + a_2(t)V_2 + \cdots + a_n(t)V_n}{A_c B_c + a_1(t)B_1 + a_2(t)B_2 + \cdots + a_n(t)B_n}, \quad (1)$$

where D is the ratio (V over B) of observed system fluxes at time t, A_c is the area of Charon, B_c and V_c are Charon's average normal reflectances in the B or V filters, the a's are

TABLE 1

OBSERVING CIRCUMSTANCES (UT TIMES)

Date	1st Contact	2nd Contact	3rd Contact	4th Contact	Time of Maximum Depth
1987 May 22[a]......	04:59	...	...	09:33	07:25
1988 Apr 18[b]	07:41	09:43	10:16	12:06	09:59
1988 Jun 21[b].......	04:36	06:29	07:11	09:21	06:50
1989 Apr 30[c]	03:51	...	...	07:26	05:41

[a] From Tholen, Buie, & Swift (1987a).
[b] From Tholen, Buie, & Swift (1987b).
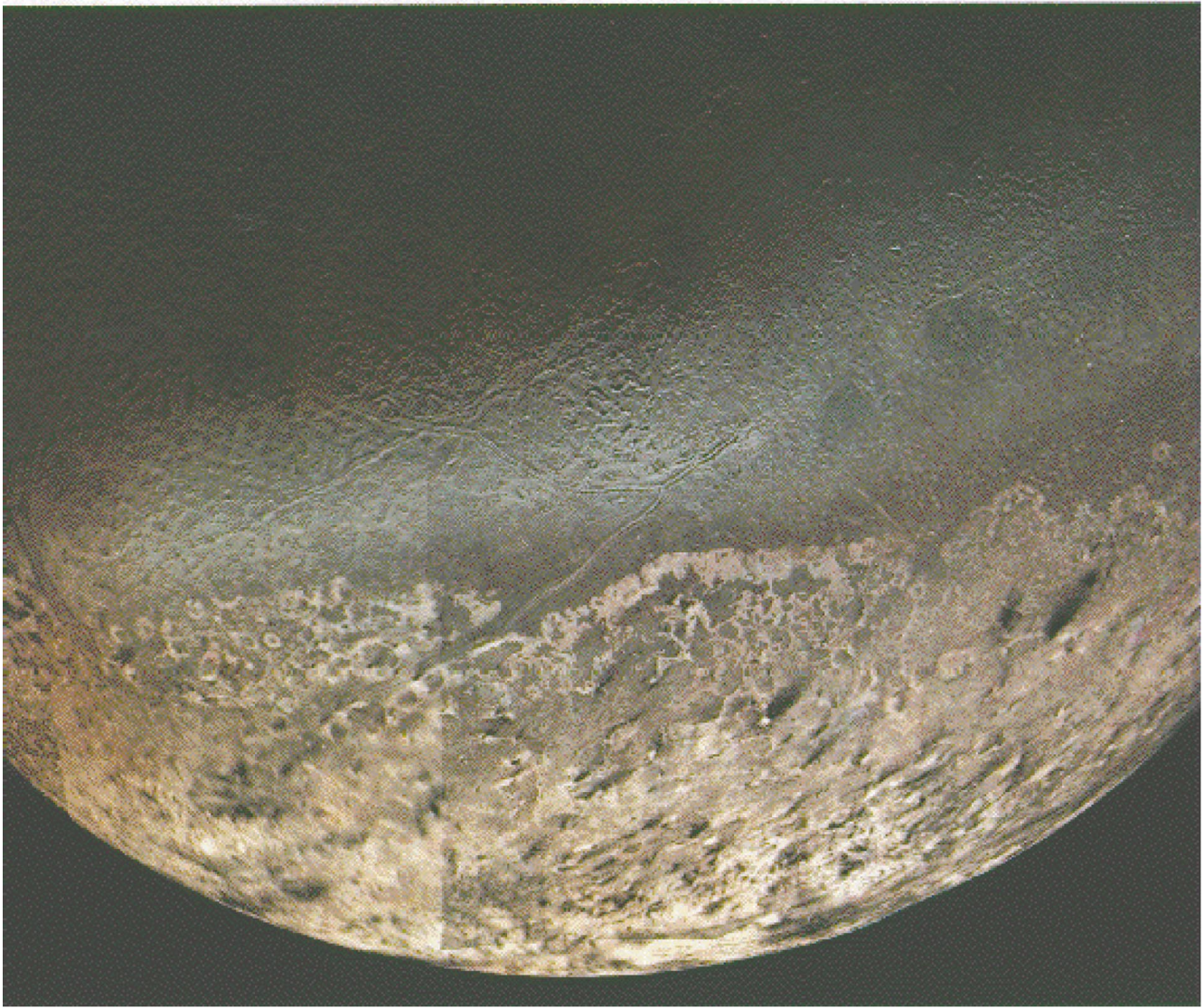[c] From Tholen & Buie (1988).

FIG. 2.—*Voyager* map of Triton. Such maps (McEwen 1990) show distinct frost regions: a relatively red south polar frost cap and a bluer "equatorial collar." The southern feature appears to be much older than the equatorial collar (Cruikshank et al. 1998).

the exposed, projected, illuminated areas of small tiles on Pluto's surface, and V_1 through V_n are the unknowns, the V-filter normal reflectances of the tiles on Pluto.

The tiles are conceptually attached to Pluto's surface. Some small change in each tile's exposed, projected area is due to Pluto's rotation, but this effect is minor, because Pluto only rotates $\sim 7°$ during a two-hour event. Most of the useful albedo information is a result of a tile being covered or uncovered by Charon or its shadow.

To recast equation (1) as a linear system of equations relating the grid elements' V reflectances to the observed V/B fluxes we multiply through by the denominator of equation (1) and subtract the constant $A_c V_c$ term from both sides.

$$D_V(t) = D(t)(A_c B_c + a_1(t)B_1 + a_2(t)B_2 + \cdots + a_n(t)B_n)$$
$$= A_c V_c + a_1(t)V_1 + a_2(t)V_2 + \cdots + a_n(t)V_n \quad (2)$$

There is no advantage to recasting equation (2) into a linear system with V/B ratios as the unknown parameters; doing so only involves scaling each a_i coefficient by a term of the form $\sum (B_n - B_i)/\sum B_n$. Instead, we generate syn-

thetic B-filter light curves from the EY99 B-filter map of Pluto. The B map is based on 18 light curves with 1977 data points, compared with only 434 data points in this two-color data set. We produce a V-flux light curve from the B-flux light curve and the $B - V$ magnitudes, then we generate separate B- and V-filter maps from B and V light curves with identical time steps (Fig. 3). The ratio of these maps serves as a two-color map.

Once we have a system in $D(t) = Fx$ form we can use the adjoint method (Claerbout 1999) to invert equation (2) robustly and to find solutions for the V- and B-flux light curves. We have taken care to propagate errors from the $B - V$ magnitude data set to the $D_V(t)$ vector that serves as V-filter "observation" vector in equation (2).

2.3. Modeling Charon's Contribution

We assume Charon's contribution is constant in both filters. Charon's geometric albedo is 0.38 in B, and Charon's $B - V$ magnitude is 0.7 with little variation at different rotational phases (Buie et al. 1997a). A solar $B - V$ magnitude of 0.62 implies a V-filter geometric albedo of 0.41 for Charon. Note that the relation between normal reflectance and geo-
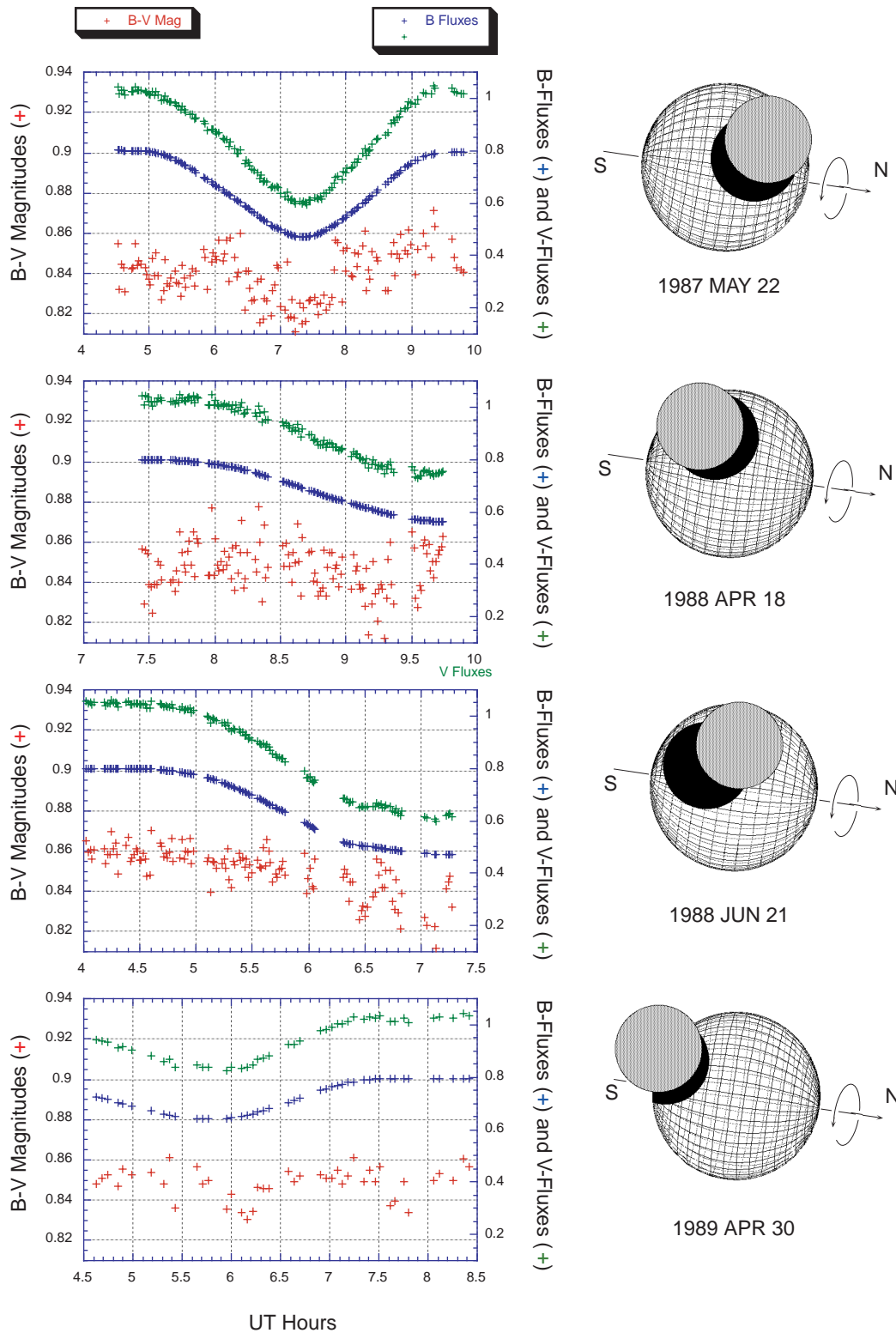
FIG. 3.—$B - V$ magnitude light curves, with B-flux and V-flux light curves. The B-flux light curve is generated by passing an existing B-map through the geometry of these four events, and the V-flux light curve is offset from the B-flux by an amount based on the $B - V$ magnitude differences. Notice that the two 1988 events were only observed through first and second contact (i.e., the ends of the transits were not observed) and that the 1989 event was picked up after first contact.

metric albedo is $r_n = (0.5 + k)p$, where r_n is normal reflectance, k is the object's Minnaert limb parameter, and p is the geometric albedo (Veverka et al. 1986).

Charon's contribution to the system flux is only approximately equal to the product of its area and normal reflec-

tance. We use an "effective area" that accounts for the scattering properties of Charon's surface. If, for example, we model Charon's limb profile with a large Minnaert coefficient (e.g., $k = 0.7$, like Europa's, resulting in a bright center and darker limb), then Charon's effective area will be less
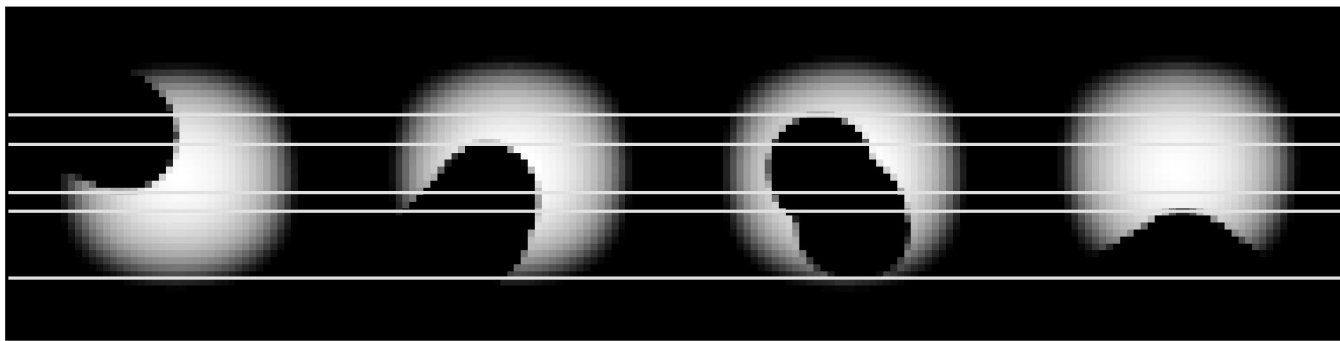
FIG. 4.—Transit paths from the four events, showing Pluto's projected disk with the coverage by Charon's disk and/or shadow. The middle two events are shown at the end of observations; if they had progressed further, Charon's obscuration would have continued to the right across Pluto's disk. In theory we can resolve latitudinal structure within the six delineated bands.

than if we had assumed a flat limb profile ($k = 0.5$, similar to the Moon's).

$$A_c = \frac{2\pi R^2}{(2k + 1)}, \qquad (3)$$

where A_c is Charon's effective area and R is Charon's radius.

Although Young & Binzel found that a set of mutual-event light curves was best fitted by a Charon limb coefficient of $k = 1.0$, they pointed out that this value is actually
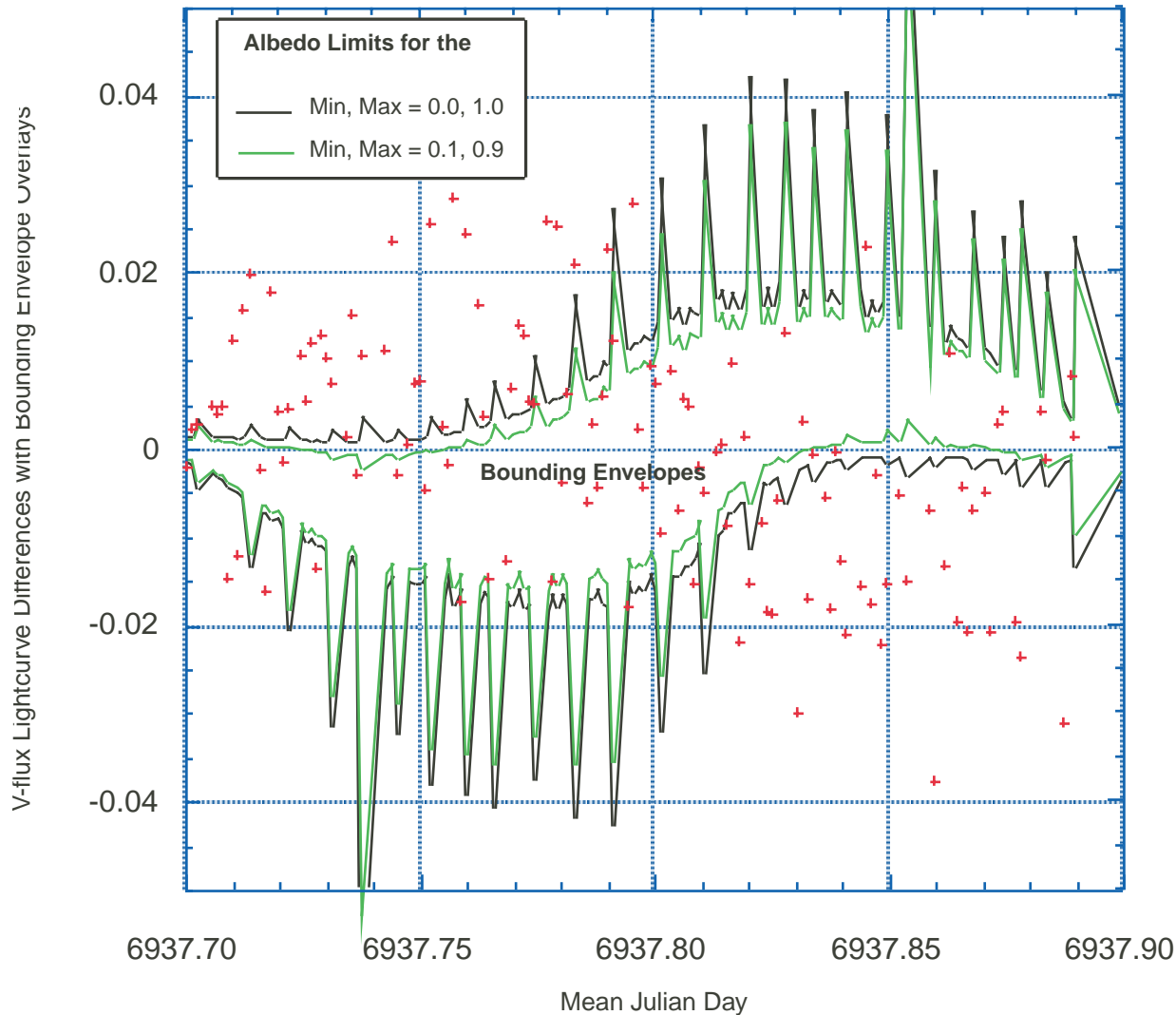

FIG. 5.—Envelopes for the light-curve differences (1987 May 22). Because each event has a U-shaped light curve, the light-curve differences should look like a sideways **S**. We generate two versions of the **S** curve, a lower and upper envelope, based on assumed lower and upper bounds on the normal reflectances on any patch on Pluto's surface. This plot shows envelopes corresponding to surface reflectance limits of 0 and 1.0 (*black*) and 0.1 to 0.9 (*green*). The overlay of the differenced data shows exactly where a pair of points is out of bounds. We can apply a constraint in difference space to the data on a pair-by-pair basis, a vast improvement over smoothing the data in the time domain.
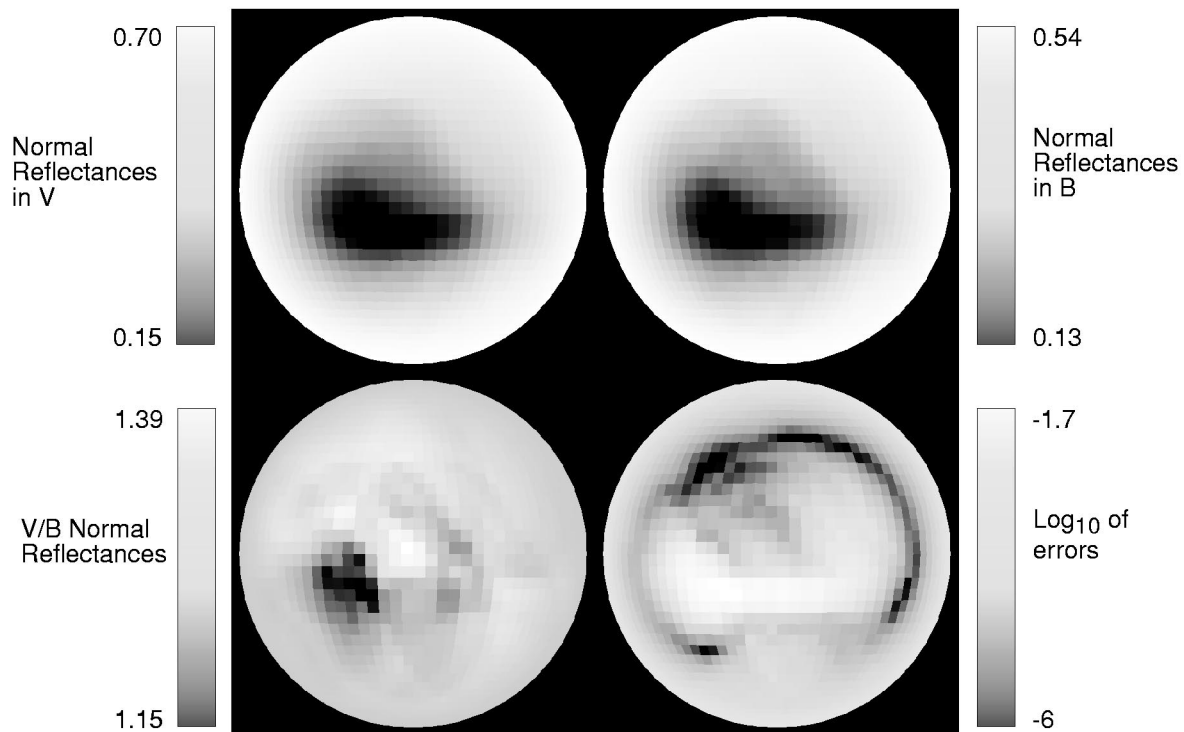
FIG. 6.—*Top left*: *B*-filter map. This map shows much less detail than the *B*-filter map used to generate synthetic light curves for this analysis (Fig. 1), because we have fewer light curves to work with, and because coverage is especially light on the right side of the disk. We can recover part of the dark subequator band (Fig. 1, feature " B ") but not much else. *Top right*: *V*-filter map. This map looks almost identical to the *B*-filter map, yet their ratio (*bottom left*) shows color structure across what we would otherwise assume to be a uniform dark band. *Bottom left*: *V/B* color map. Darker areas are less red; brighter areas are redder. Our expectation was that the subequatorial dark band would be red, but this frame shows that while the central longitudes are red, the region near W30°–W40° (*left of center*) is only slightly red, with a *V/B* reflectance ratio of 1.15. *Bottom right*: Monte Carlo error map. All errors are less than 0.02. Why are the errors highest in the regions that have the best spatial resolution? The other regions are not resolved by the events, so the adjoint method invariably assigns average *V/B* values to them. Only the central part of Pluto disk changes significantly when noise is added to the light curve. See Figs. 8 and 9 for tests of spatial resolution.

due to the combined effects of Charon's disk-averaged scattering properties and Charon's sub-Pluto albedo distribution. A value of $k = 1.0$ is unrealistic; the highest known limb parameter is 0.7 (for Europa). We chose a value of $k = 0.6$, which is the limb parameter for Titania, a Uranian satellite with a surface composition and brightness similar to Charon's.

3. THE LINEAR LIGHT CURVE INVERSION PROBLEM

The light curve inversion process we use is described in EY99; we briefly summarize it here. The basic idea is to perform a least-squares fit for the unknown V reflectances in equation (2). The design matrix a (the matrix that describes how the observations, D_V, are a linear combination of the V reflectances) is made up of the coefficients $a_1 \ldots a_n$. A straightforward inversion of equation (2) is a disaster; the results include negative normal reflectances and reflectances greater than one. This problem is caused by noise in the light curve. Because the reflectance solution is based on the differences between successive light-curve points, the solution is especially sensitive to noise. We address this problem in the manner described in EY99; namely, we use the adjoint instead of the inverse to solve equation (2) robustly, and we apply constraints on the differences as we converge on a solution.

3.1. *The Solution Using the Adjoint*

An explanation of the use of the adjoint in solving linear

problems is in Claerbout (1999).[1] For our purposes, we solve equation (2) not by inverting F but by successively applying the adjoint of F (its transpose in this case) to the residuals, the differences between D_V and the model Fx. This yields an estimate of the gradient, which we follow to find a better set of x parameters.

Unlike the inverse, the adjoint method does not arrive at the solution in a single step. Instead, the worst mismatches between data and model are resolved first, because the largest terms in the residuals are the most important in generating the gradients. After the most significant map features are found, however, the adjoint method is eventually led astray by noisy light-curve points. Some noise in the light curve is obviously noise; no real surface could generate point-to-point differences as large as some of those in our data sets. While it is possible to smooth the light curves until no illegal albedos are generated in the map solution, a better strategy is to look at the differences between successive points. Working in difference space has two advantages: the illegal (too noisy to be real) differences are both much easier to see and much easier to constrain. Figure 5 shows bounding envelopes overlaid with the actual data differences for the four events.

In EY99 we describe how we add the out-of-bounds differences to the residuals vector. When we apply the adjoint to the residuals vector, we get a modified gradient vector.

---

[1] See http://sepwww.stanford.edu/sep/prof/index.html.

One question is how much importance should be given to the out-of-bounds differences. If we weight the constraints on the differences heavily, then the resulting map is too smooth, but without enough weight to the differences constraints the map solutions will contain illegal albedos.

The weight given to the out-of-bounds part of the residuals vector is 1/10 of the weight of the regular residuals vector (the observed model part). This is close to a minimum value. No illegal albedos appeared in V- or B-map solutions with a differences weighting factor of 10%, but a weighting factor of 5% did produce negative albedos

in the maps. In EY99, the B-filter maps used a weighting factor that gave the out-of-bounds part of the residuals vector the same weight as the regular residuals vector.

4. RESULTS

Figure 6 shows the three stages of results: the B-filter map, the V-filter map, and the ratio (V/B map). A fourth frame shows the errors in the V/B map. The errors were estimated by rerunning the fitting procedure 20 times with normally distributed random noise (with the appropriate variances) added to the input light curve before calculating
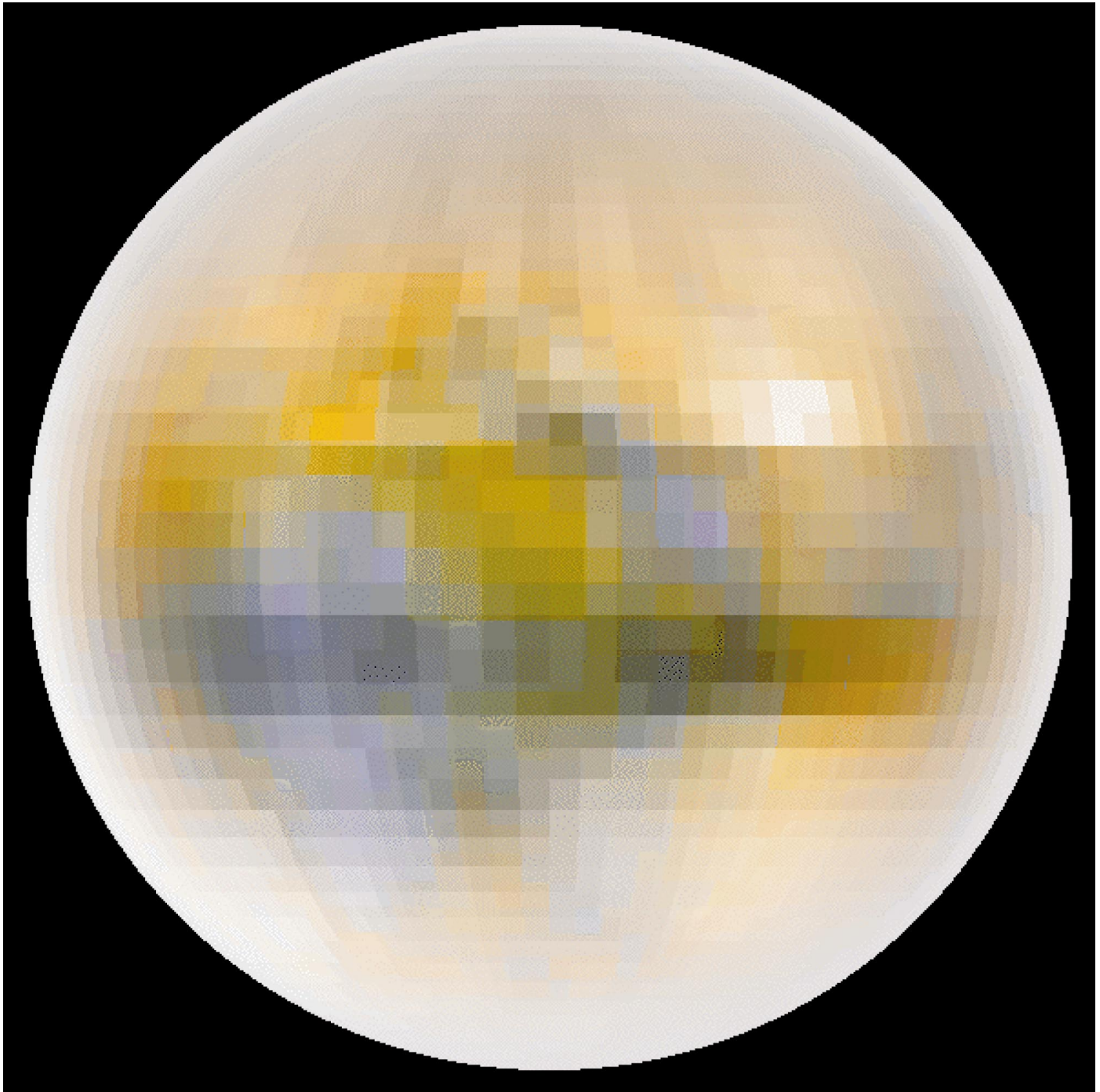

Fig. 7.—B-filter albedo map of EY99 overlaid with color information from this paper. This figure was constructed by using the B- and V-filter maps to represent blue and green channels, then manufacturing a red channel image by extrapolating the B and V differences (at 440 and 550 nm respectively) to the red (700 nm). The resulting three-color map was multiplied by the brightness map from EY99. We then increased the saturation to make colors more visible (and less realistic). Only the center of the disk has color information, and hence the grayness of the circumference.

each solution. The pixel-by-pixel rms values from the 20 solutions are the estimated errors at each pixel.

We present a color Pluto in Figure 7 for illustrative purposes only. Recall that our two channels of color are at 4400 Å and 5500 Å, blue and green, respectively, and that the average color of Pluto is rather red; hence Fig. 7 is an extrapolation in color.

5. DISCUSSION

5.1. *Spatial Resolution Tests*

The spatial resolution tests (Figs. 8 and 9) tell us which parts of the two-color map are resolved. It is disappointing that the bright albedo feature in the *B*-filter map (Fig. 1, feature "C") is not resolved, because part of the motivation for this work was to determine the color of that bright spot.

It is also apparent that we cannot resolve the southern frost cap. We can, however, resolve the dark albedo band to the north of the frost cap (Fig. 1, feature "B").

5.2. *Interpretation*

What are we to make of the fact that the dark band across Pluto (Fig. 1, feature "B") has regions of varying redness? Figure 10 plots color as a function of brightness, a crude test of the straw man hypothesis that "brighter is bluer." In fact, Figure 10 shows that brighter is not necessarily bluer. The darker pixels in our maps have a larger scatter of colors than the brighter pixels. Admittedly, there is a selection effect—the best-resolved part of the map lies over a dark albedo feature. Nonetheless, it is striking that the brighter areas (*B*-filter normal reflectances greater than ~ 0.4) have V/B reflectance ratios that are tightly clustered
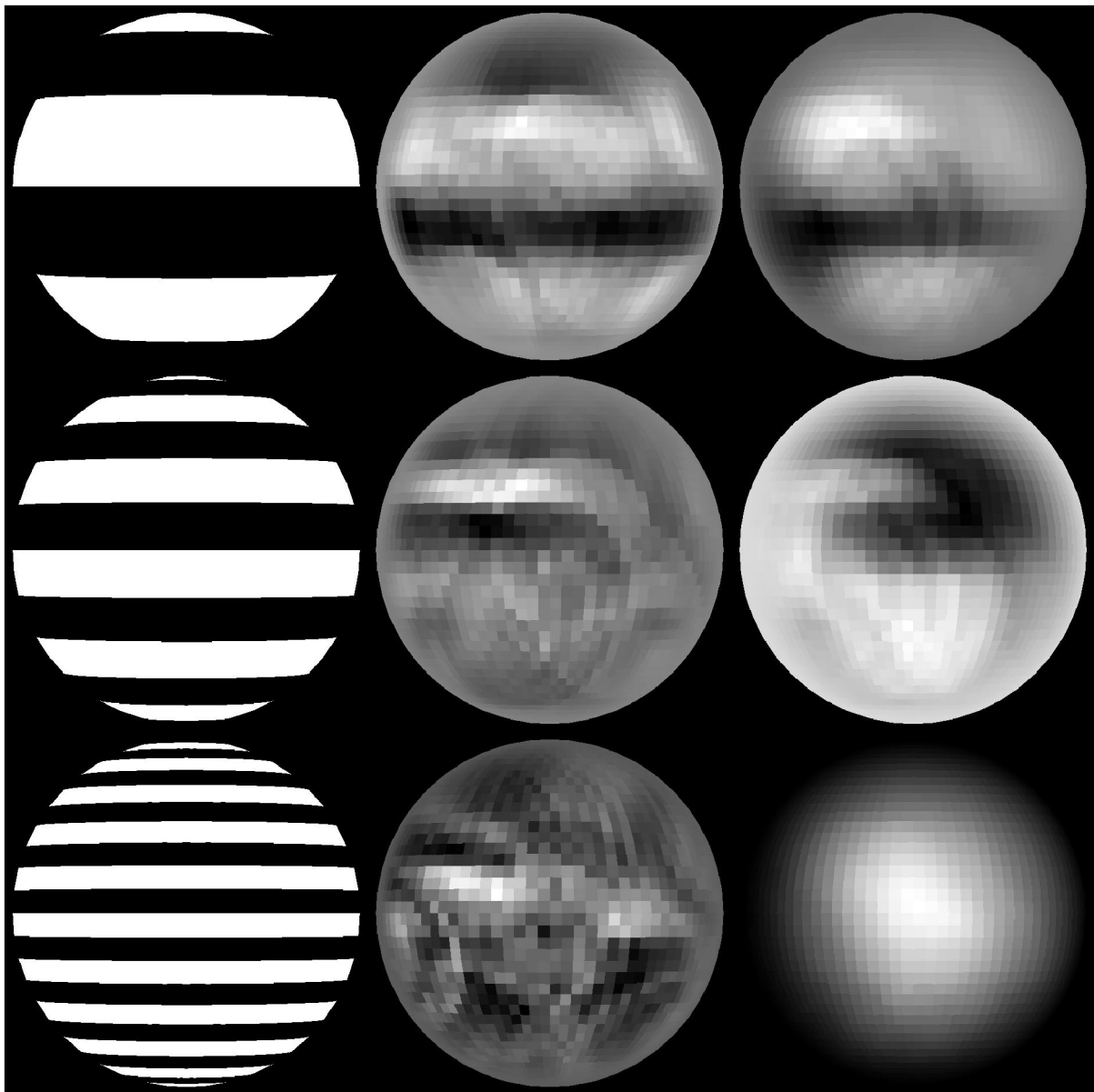

FIG. 8.—Latitudinal tests. *Left*: Original test pattern. We generated light curves (with the same time steps as the actual observations) from these patterns, then attempted to reconstruct the test patterns from the light curves. *Middle*: Reconstructions using noise-free light curves. *Right*: Reconstructions from light curves with noise added. The constraint on point-to-point differences was used in the fitting process. These tests show that we are barely able to reconstruct the six-bar pattern (*top row*). This is to be expected, because the four separate transits only distinguish six bands on Pluto's disk (see Fig. 4). The right side of the disk is not well resolved; that is where the two incomplete 1988 events do not provide coverage.
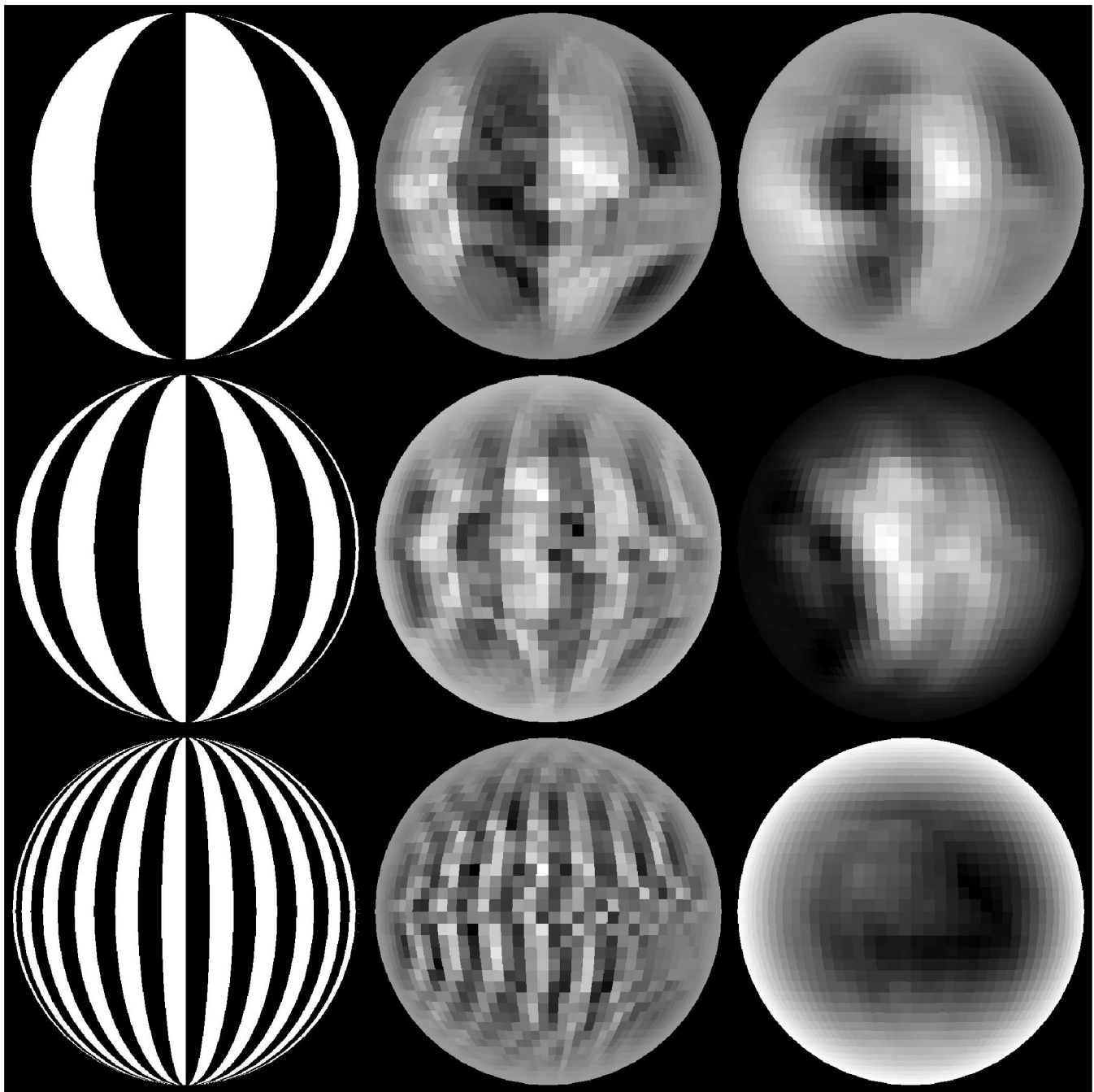
FIG. 9.—Longitudinal tests. *Left*: Original test pattern. *Middle*: Reconstructions based on noise-free light curves. *Right*: Reconstructions with noise added to the light curves. We can resolve part of the disk with 300 km longitudinal resolution (*middle row*), but 150 km resolution (*bottom row*) is out of the question.

around 1.3, when small traces of coloring agents should make a large difference in the color of bright surface frosts.

A significant part of the dark band is less red (at $B-V = 0.77$ mag. or V/B reflectance $= 1.15$) than Pluto's average $B-V$ color of 0.863 mag. although no region has been found that is bluer than the Sun's $B-V$ of 0.62 mag. Two scenarios might explain the difference in colors within the dark albedo feature. It may be that there is bright, relatively blue frost interspersed with dark material in a non-uniform way. It also may be that the dark material, which we presume to be photolysis by-products, has undergone different amounts of processing and has different intrinsic colors.

Mixed frosts.—The problem with the frost-mixed-with-dark-material scenario is that surface temperatures are expected to be higher in the neighborhood of dark material; any frost should preferentially sublimate from these regions. On the other hand, the presence of methane-rich frost regions are suspected from the overabundance of atmospheric CH_4 (Young et al. 1997). If there is frost mixed in with dark material, we would expect it to be CH_4, not N_2, because N_2 would rapidly sublimate from a region that was even a few degrees warmer than the N_2 frost global average of 40 ± 2 K (Tryka et al. 1994). In contrast, CH_4 frost at 60 K has approximately the same vapor pressure as N_2 frost at 40 K, which means that a dark, relatively warm patch of
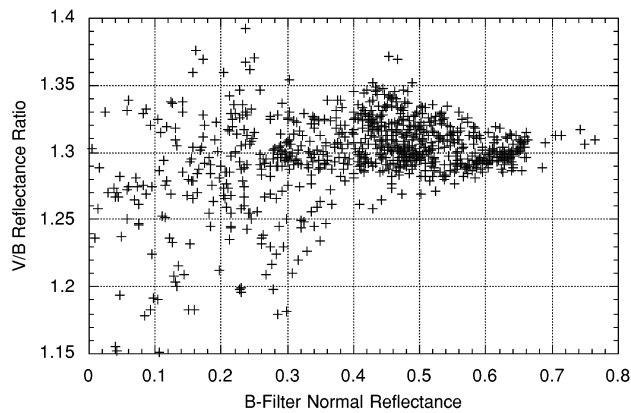
FIG. 10.—V/B reflectance ratios (redness) vs. B reflectance (brightness). Because the mutual-event light curves only let us resolve colors within the central part of Pluto's sub-Charon disk, we only plot the inner 37% of the 2304 pixels. A surprise is that the darker pixels show a greater range of colors than the brighter ones. The scatter in color is large compared with the rms errors, which are never more than 0.02.

CH_4 frost mixed with darker material could stably coexist with colder N_2 frost patches.

Photolysis by-products.—Methane dominates Pluto's solid spectrum, yet the first generation photolysis by-products C_2H_4 and C_2H_6 have not been found. The conspicuous absence of first-generation photolysis by-products on Pluto is something of a mystery, suggesting that the early by-products are short-lived. If hydrocarbons grow blacker (and less red) as they are processed by UV photolysis, then the bluer parts of the dark band could represent material that has been processed more than the redder regions. Continuing lab experiments on irradiated ices will be useful in interpreting the recent history of Pluto's surface.

REFERENCES

Bohn, R. B., Sandford, S. A., Allamandola, L. J., & Cruikshank, D. P. 1994, Icarus, 111, 151
Buie, M. W., Tholen, D. J., & Wasserman, L. H. 1997a, Icarus, 125, 233
Buie, M. W., Young, E. F., & Binzel, R. P. 1997b, in Pluto and Charon, ed. S. A. Stern & D. J. Tholen (Tucson: Univ. Arizona Press).
Claerbout, J. F. 1999, Geophysical Estimation by Example (Stanford, CA: Stanford Exploration Project)
Cruikshank, D. P., Roush, T. L., Owen, T. C., Quirico, E., & De Bergh, C. 1998, in Solar System Ices, ed. B. Schmitt, M. Festou, & C. De Bergh (Dordrecht: Kluwer)
McEwen, A. S. 1990, Geophys. Res. Lett., 17, 1765
Owen, T. C., et al. 1993, Science, 261, 745

Tholen, D. J., & Buie, M. W. 1988, AJ, 96, 1977
Tholen, D. J., Buie, M. W., & Swift, C. E. 1987a, AJ, 93, 244
———. 1987b, AJ, 94, 1681
Tryka, K. A., Brown, R. H., Cruikshank, D. P., Owen, T. C., Geballe, T. R., & Debergh, C. 1994, Icarus, 112, 513
Veverka, J., Thomas, P., Johnson, T. V., & Matson, D. 1986, in Satellites, ed J. Burns & M. Matthews (Tucson: Univ. Arizona Press)
Young, E. F., & Binzel, R. P. 1994, Icarus, 108, 219
Young, E. F., Galdamez, K., Buie, M. W., Binzel, R. P., & Tholen, D. J. 1999, AJ, 117, 1063 (EY99)
Young, L. A., Elliot, J. L., Tokunaga, A., de Bergh, C., & Owen, T. 1997, Icarus, 127, 258